Catalysis Science & Technology

ROYAL SOCIETY OF CHEMISTRY

PAPER

View Article Online
View Journal | View Issue

Cite this: *Catal. Sci. Technol.*, 2024, 14, 6015

Synergistically enhanced photoelectrocatalytic degradation of ciprofloxacin *via* oxygen vacancies and internal electric field on a $NiSe_2/WO_3$ photoanode†

Tunde L. Yusuf, *[ab] Babatope O. Ojo,[c] Talifhani Mushiana,[c] Nonhlangabezo Mabuba,[c] Omotayo A. Arotiba[c] and Seshibe Makgato[a]

This study presents the *in situ* deposition of nickel selenide ($NiSe_2$) on tungsten trioxide (WO_3) nanorods to enhance the photoelectrocatalytic degradation of organic pollutants in water. The synthesis involves integrating nickel selenide ($NiSe_2$) and tungsten trioxide (WO_3) nanorod to form a heterojunction, utilizing a facile *in situ* growth method. The resulting $NiSe_2/WO_3$ heterojunction exhibits enhanced photocatalytic properties attributed to efficient charge separation, improved charge transfer dynamics, and synergistic catalytic activity created by an internal electric field and oxygen vacancy. The heterojunction demonstrates remarkable performance in the degradation of ciprofloxacin under visible light irradiation. Under optimum conditions, the photodegradation of ciprofloxacin reached 89% (0.0179 min^{-1}) compared to pristine WO_3, which only achieved 48% (0.0069 min^{-1}) under the same conditions. The study systematically investigates the structural and morphological characteristics of the $NiSe_2/WO_3$ heterojunction and elucidates its superior photocatalytic efficacy through comprehensive experimental analyses. The primary reactive species responsible for CIP degradation were identified as photogenerated h^+ and $^{\cdot}OH$. The successful development of the $NiSe_2/WO_3$ heterojunction holds significant promise for advancing environmentally sustainable technologies in water treatment and pollution remediation.

Received 9th June 2024,
Accepted 17th August 2024

DOI: 10.1039/d4cy00729h

rsc.li/catalysis

Introduction

The dependence of humans and livestock on pharmaceuticals is increasing as the world population continues to expand. In as much as pharmaceuticals have been very beneficial, their ever-rising production and abuse of various types have raised concerns about the environment.[1,2] Numerous kinds of pharmaceutical residues have been detected in worrisome concentrations in wastewater, surface water and drinking water. Due to their adverse effects on the human population and the environment, many efforts have been made to find ways to eliminate these harmful substances from water.[3] Various techniques have been suggested, including adsorption, coagulation, flocculation, membrane filtration, chemical precipitation, ion exchange, *etc.*, to eliminate these toxic organic compounds from wastewater.[4] However, these approaches have proven ineffective and are deemed unsatisfactory due to the generation of substantial sludge requiring appropriate disposal, high operational costs, incomplete removal, and the potential production of secondary pollutants.[5,6]

Interestingly, advanced oxidation processes (AOPs), such as photocatalysis, electrochemical oxidation, photoelectrocatalysis, sonolysis, hydrodynamic cavitation and microwave oxidation, have been identified to be particularly effective for treating recalcitrant and persistent organic compounds, including pharmaceutical residues.[7–9] AOPs are innovative water treatment methods that involve the generation of highly reactive hydroxyl radicals (·OH) to break down and eliminate organic pollutants in water.[10,11] Photoelectrocatalysis is attractive because it is an AOP that synergistically combines photocatalysis and electrochemical oxidation to degrade and eliminate organic pollutants in water.[12,13] This process utilizes a semiconductor material as a photocatalyst illuminated by light to generate electron–hole pairs.[14,15] The generated charge carriers participate in electrochemical reactions, producing reactive species that can oxidize and degrade organic contaminants. Photoelectrocatalysis offers several advantages, including improved efficiency in pollutant degradation,

[a] *Department of Chemical & Materials Engineering, University of South Africa, South Africa*
[b] *Department of Chemistry, Faculty of Natural and Agricultural Sciences, University of Pretoria, Private Bag X20, Hatfield 0028, Pretoria, South Africa. E-mail: yusuf.tl@up.ac.za*
[c] *Department of Chemical Science, University of Johannesburg, South Africa*
† Electronic supplementary information (ESI) available. See DOI: https://doi.org/10.1039/d4cy00729h

enhanced control over the reaction conditions, catalyst recovery, and the potential for direct utilization of solar energy.[8,16] The efficiency of the photoelectrocatalysis process largely depends on the photoanode materials, usually semiconductors. It has been observed that photoanodes consisting of semiconductor–semiconductor heterojunctions offer higher removal efficiencies of organic pollutants in water.[17,18] Hence, there is a constant effort to develop photoanodes with appropriately matched semiconductors for photoelectrocatalytic degradation of organic pollutants.

In the pool of visible light-responsive metal oxide semiconductors, tungsten trioxide (WO_3) has garnered considerable attention as a photocatalyst in recent years, offering a promising solution for environmental remediation and sustainable energy applications.[19–21] Tungsten trioxide possesses unique properties that make it well-suited for photocatalytic applications.[22] Its semiconductor nature, high stability, and excellent light-absorbing capabilities contribute to its effectiveness in harnessing solar energy for catalytic reactions.[23,24] The various crystalline forms of WO_3, including monoclinic, hexagonal, and orthorhombic structures, add versatility to its photocatalytic performance.[25] However, while WO_3 exhibits significant promise as a photocatalyst, challenges, such as the recombination of electron–hole pairs and the need for optimal band gap engineering, persist.[25] In particular, oxygen defect modulation in WO_3 arising from heterojunction construction with suitable semiconductors is highly desired in catalytic reactions.[26] This confers a visible light response and superior charge separation advantages on the heterojunction photoanode, thus improving the overall catalytic process. Hence, to improve the photocatalytic efficiency of WO_3, research endeavours have focused on refining WO_3 band engineering by doping a heteroatom, heterojunction, or surface defects to enhance their stability for prolonged use in real-world applications.

Another promising photoelectrocatalytic material is nickel selenide ($NiSe_2$).[27] This unique material, with its distinctive properties, plays a crucial role in enhancing the efficiency and performance of photoelectrocatalytic processes.[27] As a co-catalyst, $NiSe_2$ facilitates efficient charge transfer at the semiconductor–electrolyte interface, minimizing electron–hole recombination. The material's unique electronic structure promotes rapid electron transfer, improving overall photocatalytic performance.[28] The presence of $NiSe_2$ in photoelectrocatalytic systems results in increased photocurrent and photovoltage, indicative of improved charge carrier dynamics.[27] This enhancement translates to higher efficiency in converting solar energy into chemical energy during photoelectrocatalysis. $NiSe_2$ demonstrates notable efficacy as a water-splitting co-catalyst, particularly in the hydrogen evolution reaction (HER).[29] Its electrocatalytic activity for the HER complements the photocatalytic oxidation of water, contributing to the overall efficiency of the water-splitting process.[29–31] $NiSe_2$'s versatility extends to various photocatalytic reactions beyond water splitting, including the degradation of organic pollutants and the reduction of carbon dioxide.[32,33] Its catalytic properties make it suitable for various photoelectrocatalytic applications, addressing environmental and energy-related challenges. As an emerging co-catalyst in photocatalytic applications, nickel selenide has been utilized as a co-catalyst for improving other semiconductors such as TiO_2,[34] $BiVO_4$,[34] $Cd_{0.5}Zn_{0.5}S$,[35,36] $Mn_{0.5}$-$Cd_{0.5}S$,[37] $Mn_{0.05}Cd_{0.95}S$,[38] and CdS.[28] $NiSe_2$ exhibits good stability and durability under photoelectrocatalytic conditions, ensuring prolonged and effective performance in diverse applications. Numerous studies reported in heterojunction engineering for effective acceleration of photogenerated charge separation during photoelectrocatalytic applications need consolidation. Hence, exploring the benefits of the oxygen vacancy and internal electric field in heterojunction photocatalysts to achieve charge separation and catalytic efficiency enhancement is desirable for wastewater remediation applications.

To our knowledge, $NiSe_2$ has yet to be employed as a co-catalyst to enhance the catalytic efficiency of WO_3 in degrading pharmaceuticals in water. Consequently, we present a facile synthesis method for fabricating a $NiSe_2/WO_3$ heterojunction through the *in situ* deposition of $NiSe_2$ onto WO_3. The heterojunction was sufficiently characterized by XRD, SEM, TEM, XPS, and photoelectrochemical characterization (EIS, PL, photocurrent response). The catalytic performance of the heterojunction was evaluated for the degradation of ciprofloxacin. The total organic carbon removal, degradation pathway, and detection of the reaction species are also reported.

Results and discussion

Structure, morphology, and composition

The $NiSe_2/WO_3$ heterojunction was synthesized using a solvothermal strategy, as illustrated in Scheme 1. Powder XRD was used to determine the phase purity and crystallinity of the synthesized compounds, as shown in Fig. 1a. When compared to the corresponding crystallographic planes (100), (002), (110), (102), (200), (202), and (220), the occurrence of diffraction peaks at 2θ = 14.01, 22.92, 24.33, 27.07, 28.18, 33.57, and 50.0 was well matched.[39] The peaks fall within the typical hexagonal WO_3 range (JCPDS card #33-1387), with a and c being the lattice constants. The peaks for $NiSe_2$ are almost unnoticed in the $NiSe_2/WO_3$ diffractogram due to the low concentration of $NiSe_2$ in the composite.

The morphology of the catalysts was examined using scanning electron microscopy (SEM). In the pristine WO_3, the micrographs revealed a distinct nanorod rhombohedral shape. Fig. 1b illustrates the SEM image of pristine WO_3, where cylindrical nanorods were observed in an aggregated state. However, in the SEM images of $NiSe_2/WO_3$ (Fig. 1c), the introduction of $NiSe_2$ led to a dispersed configuration of WO_3 nanorods, resulting in an increased surface area. This enhanced surface area is particularly advantageous for photocatalytic applications, increasing the active sites and overall activity. The TEM micrographs provide additional support to the findings derived from SEM analysis. In the TEM images of WO_3, an assortment of nanorods with an average diameter of 23 nm was observed. However, with the introduction of $NiSe_2$, a noticeable change occurred in the nanorod structure, characterized by

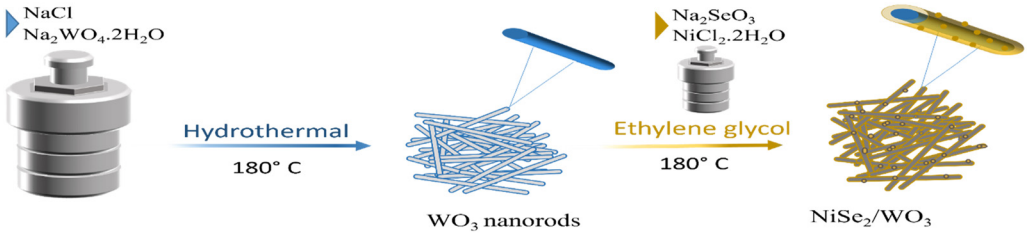

Scheme 1 Synthesis of the $NiSe_2/WO_3$ heterojunction.

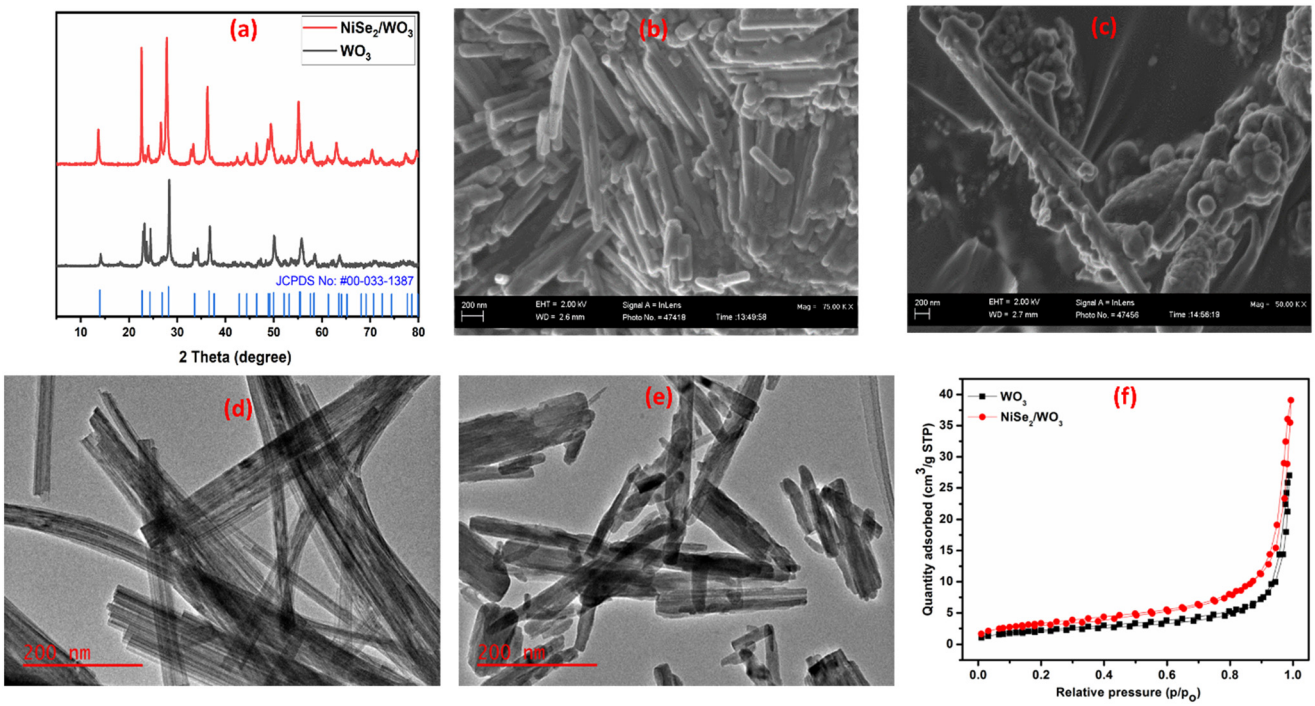

Fig. 1 a) XRD diffraction patterns of WO_3 and $NiSe_2/WO_3$, b) SEM image of WO_3, c) SEM image of $NiSe_2/WO_3$, d) TEM image of WO_3, e) TEM image of $NiSe_2/WO_3$, and (f) N_2 sorption isotherms for WO_3 and $NiSe_2/WO_3$.

breakage and a slightly increased dispersion. This suggests that the deposition of $NiSe_2$ onto the WO_3 surface enhanced the surface area by reducing the particle size. Consequently, this modification rendered the nanorods more suitable for catalytic applications.

BET analysis was also conducted to investigate the surface area enhancement emanating from the successful formation of the $NiSe_2/WO_3$ heterojunction photocatalyst. The isotherms showing the N_2 gas adsorption–desorption behaviour for WO_3 and $NiSe_2/WO_3$ photocatalysts in Fig. 1f revealed that both photocatalysts exhibited a type IV pattern. Adsorption–desorption hysteresis observed between p/p_o of 0.5–1.0 is characteristic of mesoporous materials by IUPAC classification. In particular, the surface area of 12.29 $m^2\ g^{-1}$ obtained for $NiSe_2/WO_3$ further reinforces the surface area enhancement exhibited by the $NiSe_2/WO_3$ heterojunction photocatalyst in comparison to 8.43 $m^2\ g^{-1}$ obtained for pristine WO_3. This further establishes the dispersed configuration of the synthesized $NiSe_2/WO_3$ photocatalyst, as illustrated by the SEM image. This surface enhancement underscores the successful formation of the $NiSe_2/WO_3$ heterojunction photocatalyst, bestowing tremendous benefit to the catalytic process.

The surface chemistry comprising the chemical composition and valence state of the WO_3 and $NiSe_2/WO_3$ was investigated with X-ray photoelectron spectroscopy (XPS). The total survey spectrum in Fig. 2a shows peak signals associated with the elements Ni, Se, W and O and XPS deconvoluted peaks of Se 3d, W 4d, O 1s and Ni 2p in high-resolution spectra of WO_3 and $NiSe_2/WO_3$ are presented in Fig. 2b–h. The Ni 2p characteristic peaks at approximately 856.4 and 873.8 eV are illustrative of the respective Ni $2p_{3/2}$ and Ni $2p_{1/2}$ states of Ni^{2+} in $NiSe_2/WO_3$ (Fig. 2b). Characteristics satellite peaks attributed to the Ni oxidation states were also observed at approximately 862.8 and 879.7 eV.[40] In Fig. 2c, peaks observed at approximately 53.6 and 54.3 eV correspond to Se $3d_{5/2}$ and Se $3d_{3/2}$ of the Se^{2-} anion in $NiSe_2/WO_3$, confirming the presence of the Ni–Se bond. In addition, the peak at approximately 59.1 eV can be attributed to SeO_x species, whose presence has been credited to $NiSe_2$ exposure

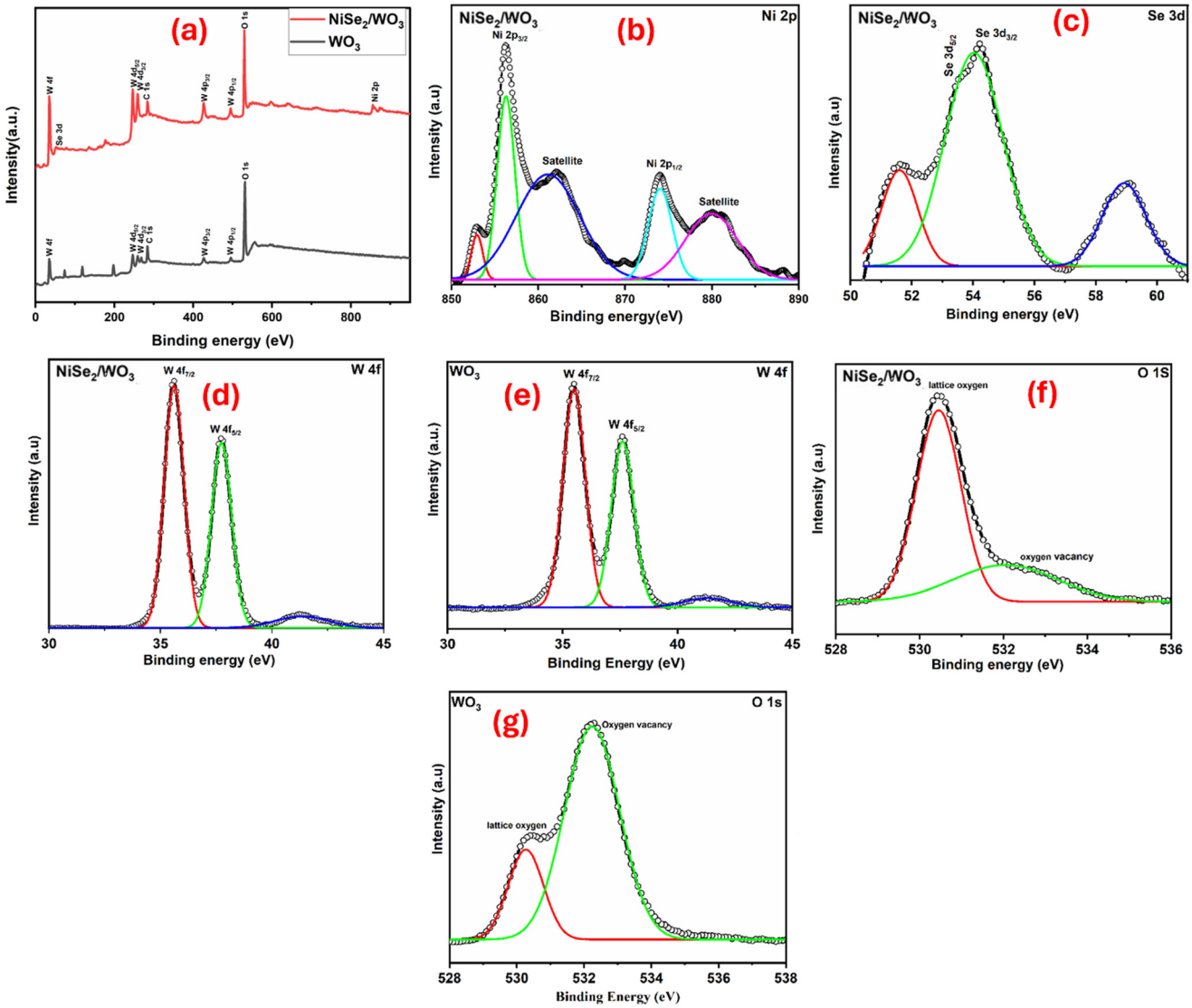

Fig. 2 (a) XPS overall survey spectra of WO_3 and $NiSe_2/WO_3$, (b) high-resolution spectra for Ni 2p in $NiSe_2/WO_3$, (c) high-resolution spectra for Se 3d in $NiSe_2/WO_3$, (d) high-resolution spectra for W 4f in $NiSe_2/WO_3$, and (e) high-resolution spectra for W 4f in WO_3. (f) High-resolution spectra for O 1s in $NiSe_2/WO_3$ and (g) high-resolution spectra for O 1s in WO_3.

to air.[41] Comparing the W 4f peaks in the high-resolution spectra of WO_3 and $NiSe_2/WO_3$ (Fig. 2d and e), characteristic peaks of W $4f_{7/2}$ and W $4f_{5/2}$ observed at approximate binding energies of 35.6 and 37.8 eV in the WO_3 spectra corresponds to the W^{6+} state.[42,43] The presence of these peaks in the high-resolution spectra of $NiSe_2/WO_3$ (Fig. 2d) further confirms the complete formation of WO_3 in $NiSe_2/WO_3$ after thermal treatment. The high-resolution O 1s spectra of $NiSe_2/WO_3$ and WO_3 showing two distinct peaks are presented in Fig. 2f and g. The intense peak at the binding energy of 530.3 eV observed for $NiSe_2/WO_3$ (Fig. 2f) can be attributed to the lattice oxygen (O^{2-}) in WO_3 of the $NiSe_2/WO_3$ heterojunction. Whereas a pronounced peak at 532.2 eV, corresponding to the oxygen vacancy, is observed in pristine WO_3 (Fig. 2g), and a significant reduction was observed in $NiSe_2/WO_3$. This suggests the occurrence of electron flow from WO_3 to $NiSe_2$ as the $NiSe_2/WO_3$ heterojunction was achieved, indicative of charge separation improvement *via* oxygen vacancy density in $NiSe_2/WO_3$.

Optical properties

Ultraviolet-visible diffuse reflectance spectroscopy (UV-DRS) is a valuable technique for determining the band gap energies of semiconductor materials and their composites. Understanding the band gap energies is crucial for optimizing their photocatalytic properties and designing efficient photocatalysts for environmental remediation and other applications. The absorption edge for WO_3 was extrapolated at 449 nm (Fig. 3a). $NiSe_2/WO_3$ exhibited a stronger absorption in the visible region, indicative of the influence of $NiSe_2$ on WO_3. The band gap energy of $NiSe_2$ typically falls in the range of 1.0 to 2.0 eV, as we

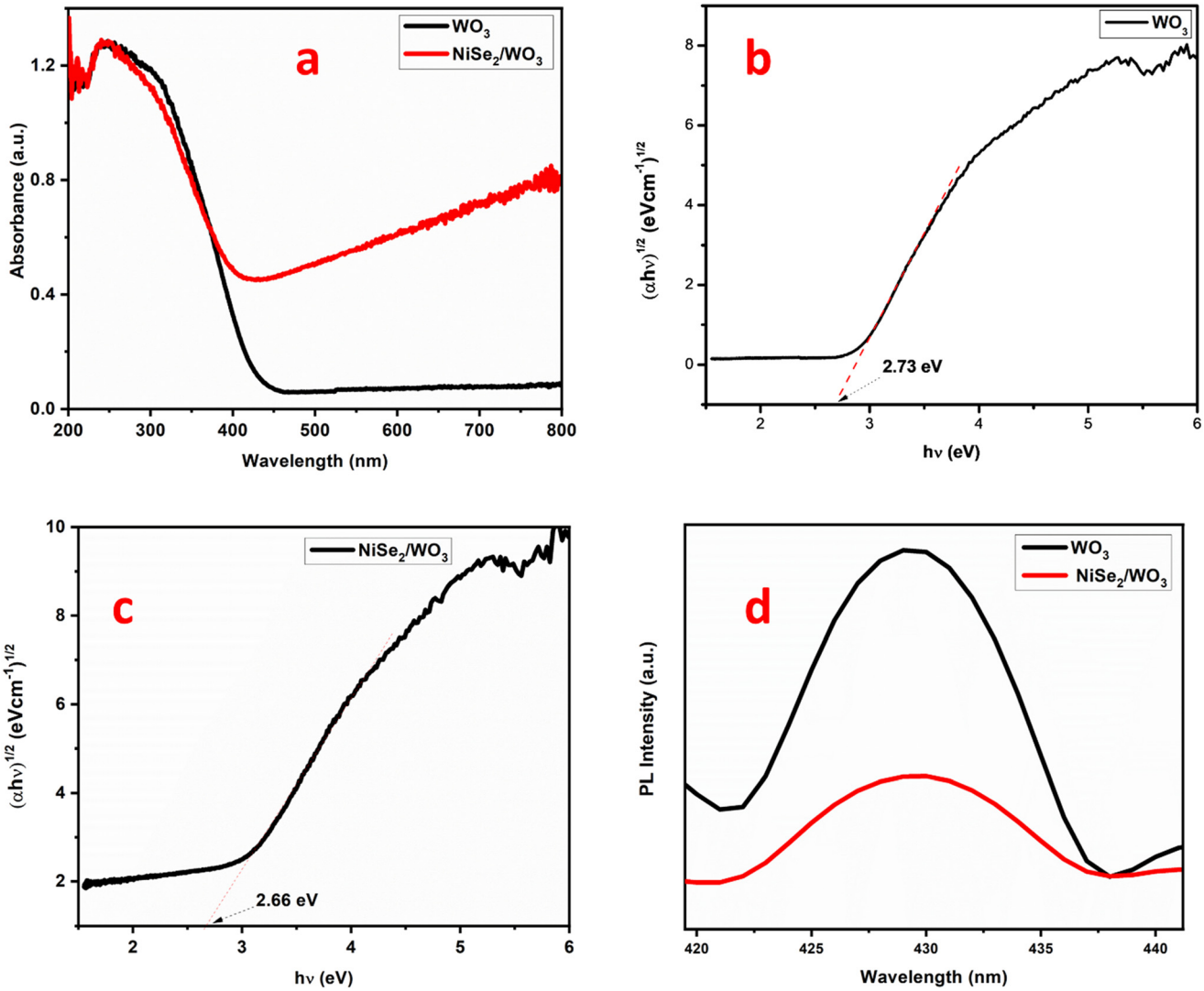

Fig. 3 a) UV-DRS spectra for WO_3 and $NiSe_2/WO_3$, b) Tauc plot for WO_3, c) Tauc plot for $NiSe_2/WO_3$, and d) photoluminescence for WO_3 and $NiSe_2/WO_3$.

have previously reported.[27] The band gaps of $NiSe_2/WO_3$ and WO_3 were calculated using the Kubelka–Munk function.

$$ahv = A(hv - E_g)^{n/2} \quad (1)$$

As depicted in Fig. 3b and c, the energy band gaps (E_g) of WO_3 were calculated as 2.73 eV, and that of $NiSe_2/WO_3$ was calculated as 2.66 eV. The valence band (VB) and the conduction band (CB) were obtained using the following equations.

$$E_{vb} = X - E^e + 0.5E_g \quad (2)$$

$$E_{cb} = E_{vb} - E_g \quad (3)$$

where E_{vb}, E_{cb}, E^e, and X represent the potential of the VB, potential of the CB, energy of free electron in the hydrogen scale (approx. 4.5 eV), and absolute electronegativity values for the semiconductor. The E_{vb} and E_{cb} are thus calculated to be +0.72 eV and +3.45 eV, respectively. The rate of photoinduced charge carrier recombination was investigated using photoluminescence spectroscopy (PL). PL can provide valuable insights into the recombination kinetics of photogenerated charge carriers in WO_3 and $NiSe_2/WO_3$ semiconductor photocatalysts. A peak displaying less intensity often depicts a suppressed charge carrier recombination rate. As illustrated in Fig. 3d, $NiSe_2/WO_3$ has the least intense peak, which implies a low charge carrier recombination rate. Therefore, incorporating $NiSe_2$ into WO_3 greatly enhanced the suppression of charge carrier recombination in the $NiSe_2/WO_3$ heterojunction.

Electrochemical and photoelectrochemical properties

Electrochemical impedance spectroscopy (EIS), a valuable technique, was employed to analyze the electrical properties of the $NiSe_2/WO_3$ semiconductor-based photocatalysts. The charge

transfer resistance (R_{ct}) at the photocatalyst–electrolyte interface is proportional to the semicircle diameter in the Nyquist plot. Whereas a larger diameter often indicates higher charge transfer resistance, a small diameter can propel the photoelectrocatalytic reaction to achieve significant efficiency. As observed in Fig. 4a, the R_{ct} of WO_3 and $NiSe_2/WO_3$ are 398.5 and 48.5 ohm, respectively, which implies that the ease of charge transfer is greater in $NiSe_2/WO_3$. The transient photocurrent density response in Fig. 4b indicates that $NiSe_2/WO_3$ possesses a significantly enhanced photocurrent response over the pristine WO_3. This further indicates that the $NiSe_2/WO_3$ heterojunction promoted a sustained charge carrier separation due to its superior visible light response edge. This superior charge-separation edge possessed by $NiSe_2/WO_3$ can promote the photoelectrocatalytic activity by prompting a significant formation of reactive species often responsible for the degradation of target organics.

Furthermore, the valence and conduction band positions of WO_3 were evaluated using the Mott–Schottky (MS) plot provided in Fig. 4c. The E–C^{-2} plot for both samples displays a positive plot, indicating n-type semiconductivity. The flat band potential obtained from the Mott–Schottky plot for WO_3 was +0.42 eV (Fig. 4c), and by employing the Nernst equation: $E_{NHE} = E_{Ag/AgCl} + 0.197$, and the E_{fb} of WO_3 is calculated to be +0.62 eV *vs.* NHE, respectively. Generally, n-type semiconductors have conduction bands of about 0.1–0.2 eV, which is more negative than the E_{fb}.[44] Therefore, the E_{cb} values for WO_3 were evaluated to be +0.72 eV *vs.* NHE. In addition, by applying the $E_{cb} = E_{vb} - E_g$ relation, the valence band (E_{vb}) for WO_3 was estimated to be 3.45 eV *vs.* NHE.

Photoelectrocatalytic performance

Degradation of ciprofloxacin. The photoelectrocatalytic degradation efficiency of the fabricated photoanode was evaluated *via* 5 mg L^{-1} CIP solution degradation with a bias potential of 1.5 V and a light source. The pristine WO_3 photoanodes achieved approximately 48% (0.0069 min^{-1})

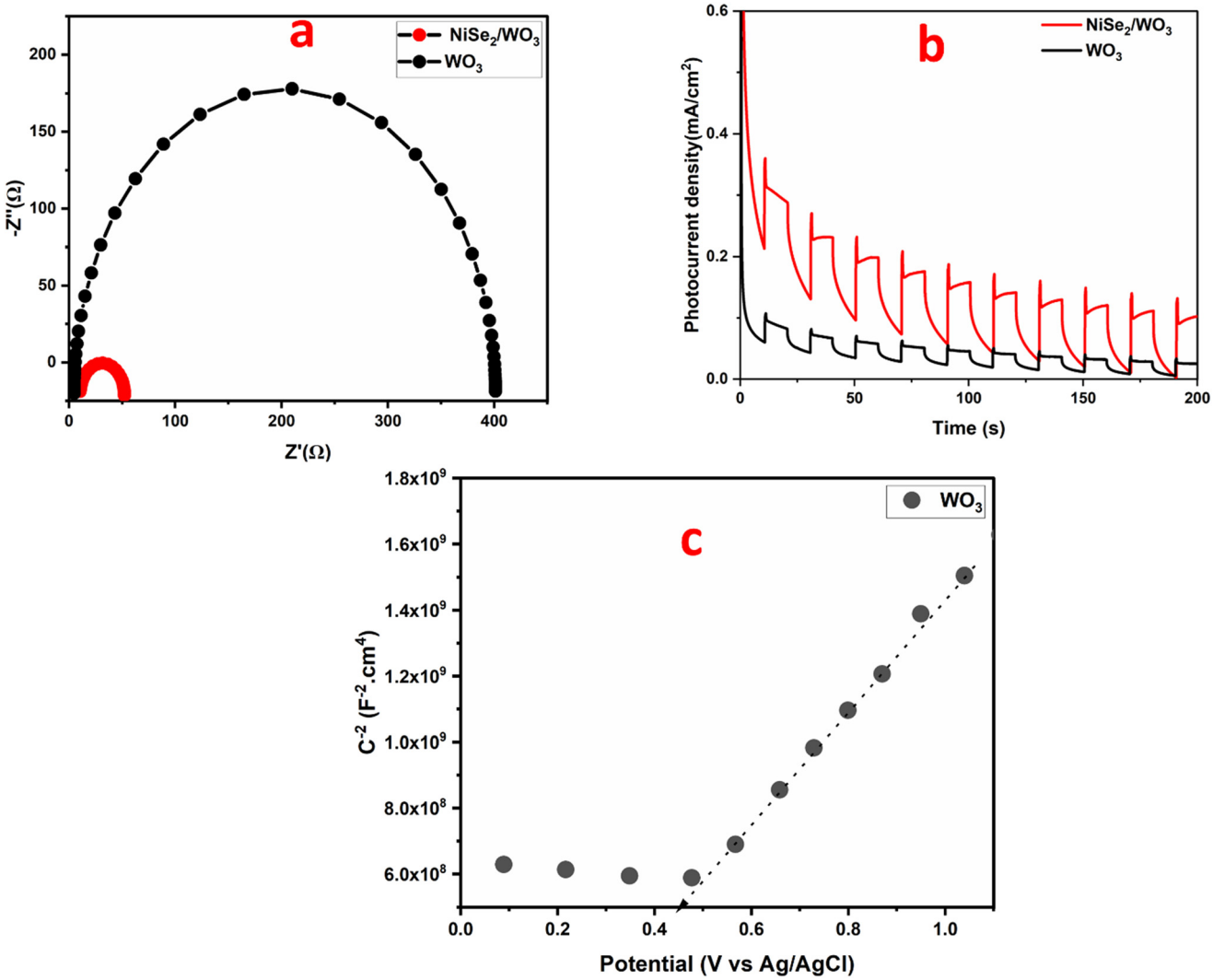

Fig. 4 (a) Nyquist plot of WO_3 and $NiSe_2/WO_3$, (b) photocurrent density of WO_3 and $NiSe_2/WO_3$, and (c) Mott–Schottky plot for WO_3.

degradation of CIP after 120 minutes (Fig. 5a and b), whereas a notable 89% (0.0179 min^{-1}) degradation was observed using the heterostructured $NiSe_2/WO_3$ photoanode within the same time interval. The reason for the enhanced performance of the $NiSe_2/WO_3$ electrode is due to the suppressed rapid recombination of photogenerated electron–hole pairs in the $NiSe_2/WO_3$ heterojunction. This agrees with the result obtained in a study conducted by Feitosa *et al.* on the photoelectrocatalytic removal of ciprofloxacin on a Fe_2O_3/BiOI@BiOBr Z-scheme heterojunction photoanode.[45] Oxygen vacancy also contributed to the improved catalytic performance of the $NiSe_2/WO_3$ photoanode by increasing the $NiSe_2/WO_3$ photoanode's affinity for adsorbed oxygen. Interestingly, oxygen affinity centers developed on catalysts through oxygen vacancy have been reported to modulate the catalytic sites by promoting electron transfer.[26,46] Furthermore, the internal electric field driven by a bias potential in the heterojunction further led to the availability of photogenerated charge carriers (holes and electrons). Consequently, the ease in active species generation arose, thus improving the degradation efficiency of the catalyst as observed for the $NiSe_2/WO_3$ heterojunction photoanode. The operating parameters and degradation efficiency of the $NiSe_2/WO_3$ photoanode compared with other photoanodes recently applied for the photoelectrocatalytic degradation of ciprofloxacin are presented in Table 1.

To assess the superiority of photoelectrocatalytic degradation over photocatalytic and electrocatalytic degradation, the $NiSe_2/WO_3$ electrode was further employed to degrade CIP under electrocatalytic and photocatalytic conditions. As shown in Fig. 5c and d, the percentage removal of the pharmaceutical was significantly reduced to 37% (0.0049 min^{-1}) and 56% (0.0073 min^{-1}) degradation in the photocatalytic and electrocatalytic processes, respectively. Evidently, the enhanced removal of CIP through the photoelectrocatalytic process arose from a synergy between the applied potential and light energy. This advantage arose from a pronounced effect exerted by the

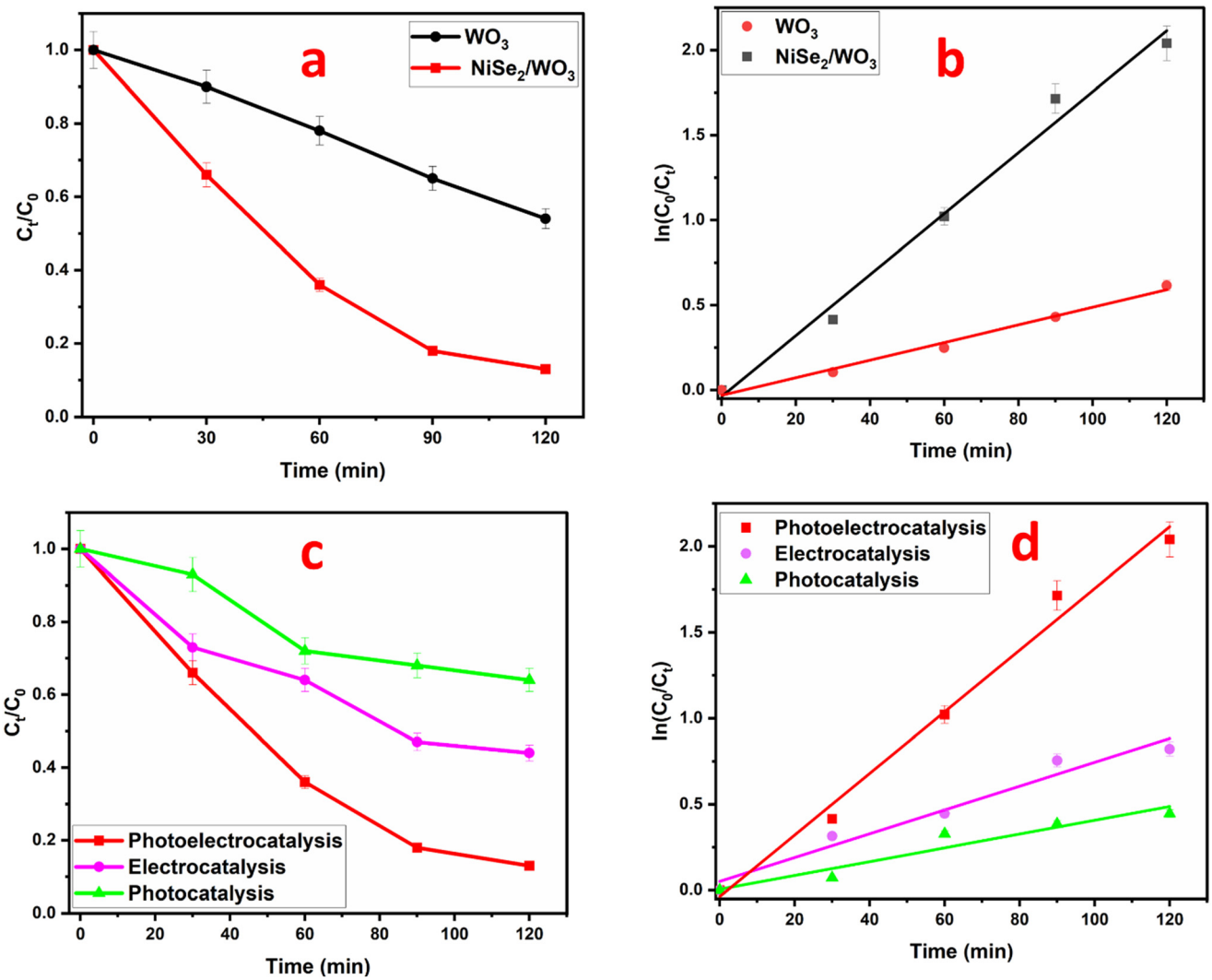

Fig. 5 (a) PEC degradation plot of CIP on MoS_2 and $NiSe_2/WO_3$ photoanodes at a 1.5 V bias potential, (b) first order kinetic plot for CIP degradation by MoS_2 and $NiSe_2/WO_3$, (c) degradation plot of CIP on NSM after photoelectrocatalytic, photocatalytic and electrocatalytic processes, and (d) first order kinetic plot of photoelectrocatalytic, photocatalytic and electrocatalytic degradation of CIP.

Table 1 Comparison of CIP degradation by recent studies on heterojunction photocatalysts

Catalysts	Process	Catalyst dosage	Pollutant	Degradation efficiency	Rate constant	Ref
FTO/Fe_2O_3/BiOI@BiOBr	Photoelectrocatalysis	Electrodeposition	Ciprofloxacin, 3.0×10^{-5} mol L^{-1}, 120 min	90%	0.07 min^{-1}	45
$NiSe_2/MoS_2$	Photoelectrocatalysis	50 mg	Ciprofloxacin, 5 mg L^{-1}, 120 min	78%	0.0111 min^{-1}	47
$TiO_2/AgBiS_2$	Photoelectrocatalysis	40 mg	Ciprofloxacin, 10 ppm, 100 min	62%	—	48
g-C_3N_4/MIL-101 (Fe)	Photoelectrocatalysis	50 mg	Ciprofloxacin, 10 mg L^{-1}, 240 min	87.6%	0.009 min^{-1}	49
$WO_3/NiSe_2$	Photoelectrocatalysis	10 mg	Ciprofloxacin, 5 mg L^{-1}, 120 min	89%	0.012 min^{-1}	This study

photocatalytic process upon illumination of the photoanode, thereby initiating the generation of charge carriers that migrate to its surface. The resulting holes oxidize CIP and interact with water molecules, yielding highly oxidizing hydroxyl radicals, further aiding CIP degradation. However, the occurrence of charge carrier recombination hindered this process, resulting in reduced degradation efficiency. Nonetheless, the presence of the bias potential aided charge carrier separation as electrons travel through the circuit to the cathode, reducing recombination rates. The observed variation in the apparent first-order rate constants ($NiSe_2/WO_3 > WO_3$) further highlights the superior efficiency of the $NiSe_2/WO_3$ heterojunction photoanode.

Effect of different applied potentials and initial concentrations. It is crucial to assess the impact of the bias potential on the photoelectrochemical (PEC) degradation process, as this potential can facilitate the separation of charge carriers. Fig. 6a illustrates the effect of various applied potentials on the photoelectrochemical degradation process. A progressive enhancement in degradation efficiency is observed with incremental increases in the potential. Notably, the efficiency experiences a significant surge from 1.0 to 1.5 V. Subsequent increase was observed at 1.8 V, albeit at a negligible rate, likely due to the influence of oxygen-trapped bubbles generation at higher potentials at the photoanode. This phenomenon may weaken the availability of hydroxyl radicals and other generated species, which are crucial for the degradation of the target pollutants' photoelectrocatalytic activity. Consequently, a potential of 1.5 V is maintained throughout this study. Likewise, the effect of varying initial concentrations of CIP during PEC degradation was observed on the $NiSe_2/WO_3$ photoanode. A proportionate decrease in the degradation efficiency from 89% to 70% was obtained with an increased initial concentration of CIP from 3 mg L^{-1} to 10 mg L^{-1} (Fig. 6b). This event can be influenced by an increased amount of CIP engaging a constant surface area of the $NiSe_2/WO_3$ photoanode when the initial concentration of CIP is increased. Hence, this result signals the photoanode's enormous capacity to destroy a wide range of recalcitrant organic pollutants often detected in various water bodies.

Stability and scavenger studies. The stability of the $NiSe_2/WO_3$ photoanode was evaluated by subjecting it to six cycles of the PEC process. The photoanode displayed remarkable stability upon its application for six PEC degradation cycles (Fig. 6c). With an average degradation efficiency of 84% after 720 min, the photocatalyst proves to possess a phenomenal ability to destroy a wide range of organic pollutants under different operational conditions. Furthermore, the stability of the heterojunction was verified post-catalysis. The XRD spectra of the catalyst showed no significant changes before and after use, confirming its stability (Fig. 6e). In addition, this performance confirms a sustained charge carrier separation in the $NiSe_2/WO_3$ heterojunction throughout the period. Moreover, photogenerated species h^+, $^{\bullet}OH$ and $O_2^{\bullet-}$ were individually trapped using ethylene diamine (EDTA-Na), *tert*-butanol and acrylamide, respectively (Fig. 6d) to detect the species responsible for the degradation of CIP. Introducing *tert*-butanol into the bulk solution resulted in a degradation efficiency of 16%, indicating that photogenerated $^{\bullet}OH$ radicals played a significant role in the degradation of ciprofloxacin (CIP). This finding supports the successful charge carrier separation in the $NiSe_2/WO_3$ photoanode during the PEC process. Additionally, using EDTA-Na as a scavenger for photogenerated holes resulted in a 37% degradation efficiency, demonstrating that the photogenerated h^+ was also crucial for CIP degradation. Furthermore, a degradation efficiency of 77% obtained with the introduction of acrylamide into the PEC system showed that photogenerated $^{\bullet}O^{2-}$ did not play a significant role in the degradation of CIP.

Mechanism of the PEC degradation process. The mechanism of the PEC reaction illustrating the band alignment scheme and the formation of the n–n heterojunction is presented in Fig. 7. Prior to the heterojunction formation, positions of the conduction and valence band potentials seem unfit for the PEC activity. However, upon constructing the $NiSe_2/WO_3$ heterojunction, charge carrier redistribution between the WO_3 and $NiSe_2$ structural interface was achieved. The heterojunction photoanode followed an electron flow from WO_3 to $NiSe_2$ due to the oxygen vacancy of WO_3. The availability of unpaired electrons indicated by this surface defect resulted in an accumulation layer near the surface region, as confirmed by the O 1s spectrum of WO_3. Consequently, a downward band movement towards a more positive potential arose in WO_3, modulating the surface activity of the synthesized $NiSe_2/WO_3$.

Moreover, the internal electric field driven by the bias potential in the heterojunction further led to electron flow from the conduction band of WO_3 to the valence band of $NiSe_2$. Thus, establishing the availability of photogenerated charge carriers (holes and electrons) in the PEC process

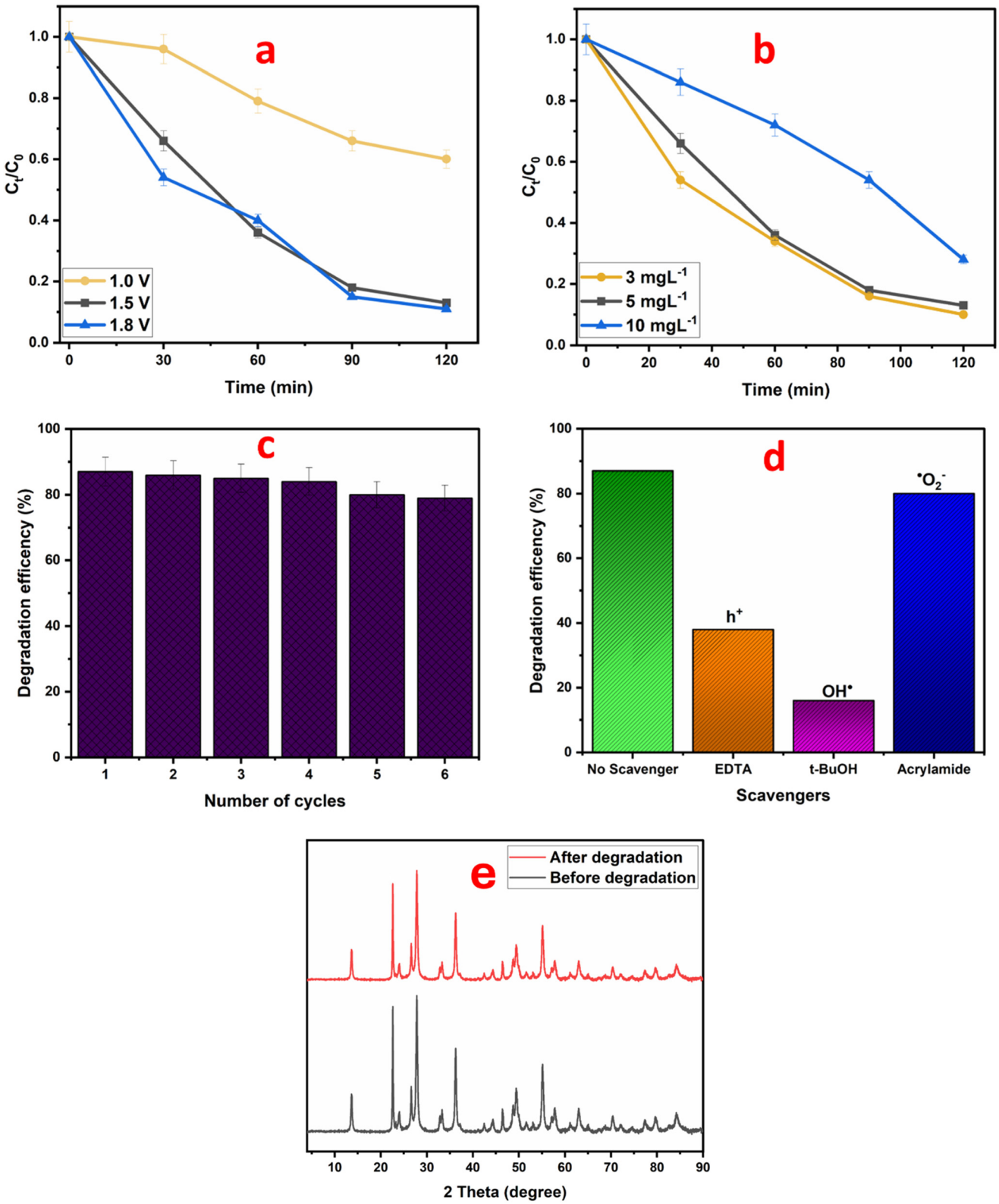

Fig. 6 (a) PEC degradation plot of CIP at different applied bias potentials, (b) PEC degradation plot at different initial concentrations of CIP, (c) reusability study plot of $NiSe_2/WO_3$ photoanode after six cycles, and (d) scavenger study plot of the photogenerated species during PEC process. (e) XRD diffractogram for $NiSe_2/WO_3$ before and after PEC degradation.

produced hydroxyl, which is primarily responsible for the degradation of CIP. This charge-redistribution mechanism agrees with the XPS high-resolution O 1s spectra (Fig. 2f and g) and the scavenger study (Fig. 6d). Eqn (4)–(6)

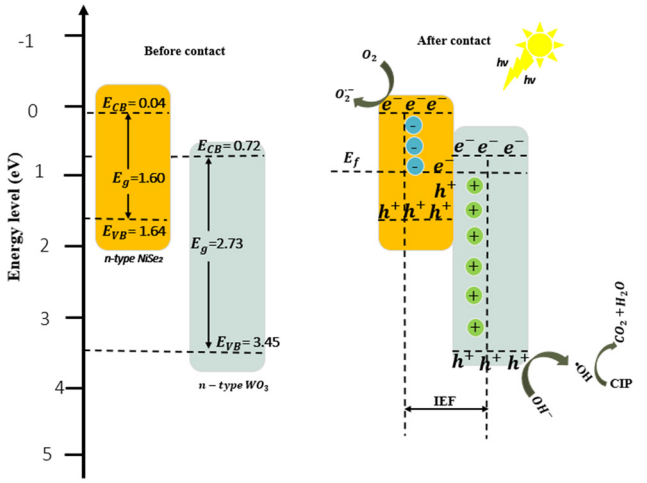

Fig. 7 Proposed mechanism for the PEC degradation of CIP.

represent reactions establishing the photoelectrocatalytic activity *via* the $NiSe_2/WO_3$ heterojunction photoanode.

$$NiSe_2/WO_3 + Vis \rightarrow h^+ + e^- \quad (4)$$

$$H_2O + h^+ \rightarrow {}^{\bullet}OH + H+ \quad (5)$$

$${}^{\bullet}OH + h^+ + CIP \rightarrow Byproducts + H_2O + CO_2 \quad (6)$$

PEC degradation pathway of CIP on the $NiSe_2/WO_3$ anode. The proposed degradation pathway of degraded CIP was obtained from chromatograms acquired from UPLC-MS analysis performed on the analyte solution during and after PEC degradation analysis. As presented in Fig. S1,† a prominent peak of m/z = 332 was obtained from the standard solution of CIP. In contrast, ion peaks of m/z = 306, m/z = 288 and m/z = 164, corresponding to different intermediate products, were obtained from the mass spectra of the degraded analyte at a different operational time during the degradation of CIP. These peaks conform to ion peaks often reported during CIP degradation.[50,51] Based on the intermediates identified in Fig. 8, the first degradation path (route I–IV) involves the decarboxylation of the carboxylic group on the quinolone moiety of CIP (route I–II).[52] This was followed by eliminating the piperazinyl ring and the fluorine atom on the quinolone moiety (route II–III). Further oxidation of the quinolone moiety resulted in ring opening and subsequent formation of aldehyde and amide attachments on the benzene ring (route III–IV). Furthermore, a second degradation path involving double oxidation of the piperazinyl ring was identified in route I–V. Consequently, the oxidation actions resulted in the formation of an amine attachment on the quinolone moiety (route I–V) and the removal of the fluorine atom from the quinolone moiety (route V–VI).[50,53]

Moreover, the opened piperayl ring was oxidized to form an amide attachment on the quinolone moiety (V–VII). These intermediates can undergo further oxidation to form CO_2, H_2O, and NH_3. The formation of these identified by-products further substantiates the superior suppression of charge carrier recombination during the process, thus leading to the sustained generation of species responsible for the decomposition of CIP and improved PEC activity.

Conclusions

In summary, we present a systematic strategy for removing CIP *via* an improved photoelectrocatalytic approach using a nickel selenide–tungsten trioxide heterojunction. The heterostructured $NiSe_2/WO_3$ band gap was effectively narrowed through a precise

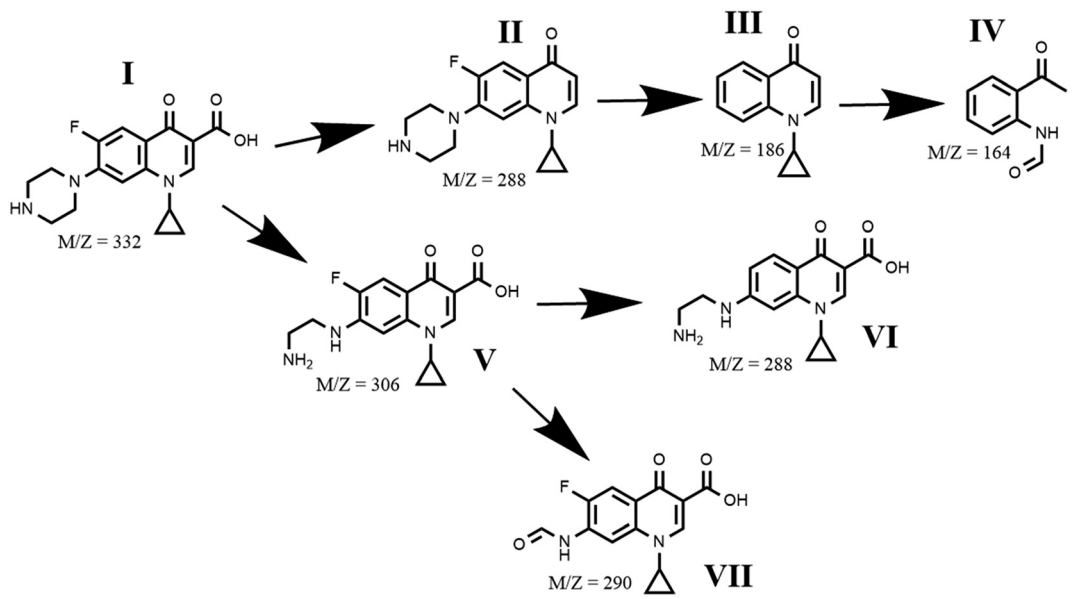

Fig. 8 Proposed degradation pathway showing byproducts I–VII for the CIP PEC process at the $NiSE_2/WO_3$ photoanode.

composite formation. Consequently, the recombination of photogenerated charge carriers was significantly suppressed while achieving a significant improvement in charge-transfer efficiency as established by the optical and electrochemical properties of the photoactive composite. Moreover, these advantages improved the kinetics of the reaction and degradation efficiency of ciprofloxacin during the photoelectrocatalytic process. Furthermore, the heterostructured photoanode demonstrated a markedly substantial degradation efficiency at a low bias potential against higher initial concentrations of CIP. The scavenger analysis of the study revealed that hydroxyl and superoxide radicals generated from the interaction of photogenerated charge carriers with hydroxyl ions and oxygen were primarily responsible for the degradation of CIP. Our investigation provides a robust framework for optimising photoelectrochemical energy conversion, capitalizing on exploiting solar illumination and low bias potential for water remediation.

Data availability

The data supporting this study's findings are available from the corresponding author upon reasonable request. The datasets generated during and/or analyzed during the current study are not publicly available but are available from the corresponding author on reasonable request. Additionally, supplementary data and materials can be found in the ESI† files associated with this publication.

Conflicts of interest

There are no conflicts to declare.

Acknowledgements

We are grateful to the University of Pretoria, the University of Johannesburg and the University of South Africa for providing the facility for this research. BO is grateful to URC, University of Johannesburg, for the award of a postdoctoral fellowship.

References

1 J.-L. Liu and M.-H. Wong, *Environ. Int.*, 2013, **59**, 208–224.
2 P. Chaturvedi, P. Shukla, B. S. Giri, P. Chowdhary, R. Chandra, P. Gupta and A. Pandey, *Environ. Res.*, 2021, **194**, 110664.
3 K. Kümmerer, *J. Environ. Manage.*, 2009, **90**, 2354–2366.
4 A. Saravanan, P. S. Kumar, S. Jeevanantham, S. Karishma, B. Tajsabreen, P. Yaashikaa and B. Reshma, *Chemosphere*, 2021, **280**, 130595.
5 T. A. Saleh, M. Mustaqeem and M. Khaled, *Environ. Nanotechnol., Monit. Manage.*, 2022, **17**, 100617.
6 P. Rajasulochana and V. Preethy, *Resour.-Effic. Technol.*, 2016, **2**, 175–184.
7 E. Brillas, I. Sirés and M. A. Oturan, *Chem. Rev.*, 2009, **109**, 6570–6631.
8 T. L. Yusuf, B. O. Orimolade, D. Masekela, B. Mamba and N. Mabuba, *RSC Adv.*, 2022, **12**, 26176–26191.
9 O. C. Olatunde, T. L. Yusuf, N. Mabuba, D. C. Onwudiwe and S. Makgato, *J. Water Process Eng.*, 2024, **59**, 105074.
10 M. Cheng, G. Zeng, D. Huang, C. Lai, P. Xu, C. Zhang and Y. Liu, *Chem. Eng. J.*, 2016, **284**, 582–598.
11 Q. Yang, Y. Ma, F. Chen, F. Yao, J. Sun, S. Wang, K. Yi, L. Hou, X. Li and D. Wang, *Chem. Eng. J.*, 2019, **378**, 122149.
12 P. Alulema-Pullupaxi, P. J. Espinoza-Montero, C. Sigcha-Pallo, R. Vargas, L. Fernandez, J. M. Peralta-Hernandez and J. L. Paz, *Chemosphere*, 2021, **281**, 130821.
13 S. Garcia-Segura and E. Brillas, *J. Photochem. Photobiol., C*, 2017, **31**, 1–35.
14 J. D. García-Espinoza, I. Robles, A. Durán-Moreno and L. A. Godínez, *Chemosphere*, 2021, **274**, 129957.
15 E. Mousset and D. D. Dionysiou, *Environ. Chem. Lett.*, 2020, **18**, 1301–1318.
16 T. Mohlala, T. L. Yusuf and N. Mabuba, *J. Electroanal. Chem.*, 2023, **947**, 117806.
17 T. L. Yusuf, S. A. Ogundare, F. Opoku and N. Mabuba, *Surf. Interfaces*, 2023, **36**, 102534.
18 K. D. Jayeola, D. S. Sipuka, T. I. Sebokolodi, O. V. Nkwachukwu, C. Muzenda, B. A. Koiki, J. O. Babalola, M. Zhou and O. A. Arotiba, *Chem. Eng. J.*, 2024, **479**, 147482.
19 J. Murillo-Sierra, A. Hernández-Ramírez, L. Hinojosa-Reyes and J. Guzmán-Mar, *Chem. Eng. J. Adv.*, 2021, **5**, 100070.
20 V. Dutta, S. Sharma, P. Raizada, V. K. Thakur, A. A. P. Khan, V. Saini, A. M. Asiri and P. Singh, *J. Environ. Chem. Eng.*, 2021, **9**, 105018.
21 M. G. Peleyeju and E. L. Viljoen, *J. Water Process Eng.*, 2021, **40**, 101930.
22 S. Adhikari, K. S. Chandra, D.-H. Kim, G. Madras and D. Sarkar, *Adv. Powder Technol.*, 2018, **29**, 1591–1600.
23 O. Samuel, M. H. D. Othman, R. Kamaludin, O. Sinsamphanh, H. Abdullah, M. H. Puteh and T. A. Kurniawan, *Ceram. Int.*, 2022, **48**, 5845–5875.
24 S. Adhikari, M. Murmu and D. H. Kim, *Small*, 2022, **18**, 2202654.
25 P. Shandilya, S. Sambyal, R. Sharma, P. Mandyal and B. Fang, *J. Hazard. Mater.*, 2022, **428**, 128218.
26 M. Zhang, D. Wang, H. Ma, H. Wei and G. Wang, *Sci. Total Environ.*, 2024, **924**, 171383.
27 T. L. Yusuf, S. A. Ogundare, F. Opoku, O. A. Arotiba and N. Mabuba, *J. Environ. Chem. Eng.*, 2023, **11**, 110711.
28 S. Shen, L. Yan, K. Song, Z. Lin, Z. Wang, D. Du and H. Zhang, *RSC Adv.*, 2020, **10**, 42008–42013.
29 I. H. Kwak, H. S. Im, D. M. Jang, Y. W. Kim, K. Park, Y. R. Lim, E. H. Cha and J. Park, *ACS Appl. Mater. Interfaces*, 2016, **8**, 5327–5334.
30 L. Yang, L. Huang, Y. Yao and L. Jiao, *Appl. Catal., B*, 2021, **282**, 119584.
31 C. Liu, T. Gong, J. Zhang, X. Zheng, J. Mao, H. Liu, Y. Li and Q. Hao, *Appl. Catal., B*, 2020, **262**, 118245.
32 C. Yang, Y. Lu, W. Duan, Z. Kong, Z. Huang, T. Yang, Y. Zou, R. Chen and S. Wang, *Energy Fuels*, 2021, **35**, 14283–14303.

33 X. Xia, L. Wang, N. Sui, V. L. Colvin and W. Y. William, *Nanoscale*, 2020, **12**, 12249–12262.
34 S. Shen, H. Zhang, A. Xu, Y. Zhao, Z. Lin, Z. Wang, W. Zhong and S. Feng, *J. Alloys Compd.*, 2021, **875**, 160071.
35 X. Zhang, Z. Cheng, P. Deng, L. Zhang and Y. Hou, *Int. J. Hydrogen Energy*, 2021, **46**, 15389–15397.
36 H. Gong, Z. Li, Z. Chen, Q. Liu, M. Song and C. Huang, *ACS Appl. Nano Mater.*, 2020, **3**, 3665–3674.
37 X. Jiang, H. Gong, Q. Liu, M. Song and C. Huang, *Appl. Catal., B*, 2020, **268**, 118439.
38 H. Liu, T. Yan, Z. Jin and Q. Ma, *New J. Chem.*, 2020, **44**, 14879–14889.
39 V. Ramar and K. Balasubramanian, *ACS Appl. Nano Mater.*, 2021, **4**, 5512–5521.
40 K. Lu, J. Sun, H. Xu, C. Jiang, W. Jiang, F. Dai, H. Wang and H. Hao, *Mater. Adv.*, 2022, **3**, 2139–2145.
41 Z. Li, X. Ma, L. Wu, H. Ye, L. Li, S. Lin, X. Zhang, Z. Shao, Y. Yang and H. Gao, *RSC Adv.*, 2021, **11**, 6842–6849.
42 M. Tong, J. Yang, Q. Jin, X. Zhang, J. Gao and G. Li, *J. Mater. Sci.*, 2019, **54**, 10656–10669.
43 A. K. Mohamedkhair, Q. A. Drmosh, M. Qamar and Z. H. Yamani, *Catalysts*, 2021, **11**, 381.
44 X. Yue, S. Yi, R. Wang, Z. Zhang and S. Qiu, *Nano Energy*, 2018, **47**, 463–473.
45 M. H. A. Feitosa, A. M. Santos, A. Wong, C. A. F. Moraes, G. M. Grosseli, O. R. Nascimento, P. S. Fadini and F. C. Moraes, *Chem. Eng. J.*, 2024, **493**, 152291.
46 X. Li, Q. Liu, F. Deng, J. Huang, L. Han, C. He, Z. Chen, Y. Luo and Y. Zhu, *Appl. Catal., B*, 2022, **314**, 121502.
47 T. L. Yusuf, O. C. Olatunde, D. Masekela, K. D. Modibane, D. C. Onwudiwe and S. Makgato, *ChemElectroChem*, 2024, e202400309.
48 Laxmiputra, D. B. Nityashree, Udayabhanu, S. M. Anush, K. Pramoda, K. Prashantha, B. U. M. B N, Y. R. Girish and H. Nagarajaiah, *Mater. Res. Bull.*, 2024, **169**, 112489.
49 H. Liu, C. Du, M. Li, S. Zhang, H. Bai, L. Yang and S. Zhang, *ACS Appl. Mater. Interfaces*, 2018, **10**, 28686–28694.
50 Z. Chen, W. Lai, Y. Xu, G. Xie, W. Hou, P. Zhanchang, C. Kuang and Y. Li, *J. Hazard. Mater.*, 2021, **405**, 124262.
51 Z. Jia, R. Lv, L. Guo, J. Zhang, R. Li, J. Liu and C. Fan, *Sep. Purif. Technol.*, 2021, **257**, 117872.
52 C. Wang, T. Zhang, J. Luo, M. Wu, J. Niu, E. Shang, C. Ni and J. Ni, *Sep. Purif. Technol.*, 2022, **297**, 121528.
53 M. Sayed, M. Ismail, S. Khan, S. Tabassum and H. M. Khan, *Environ. Technol.*, 2016, **37**, 590–602.

